Saturation wind power potential and its implications for wind energy

Mark Z. Jacobson[a,1] and Cristina L. Archer[b,1]

[a]Department of Civil and Environmental Engineering, Stanford University, Stanford, CA 94305-4020; and [b]College of Earth, Ocean, and Environment, University of Delaware, Newark, DE 19716

Edited by Michael B. McElroy, Harvard University, Cambridge, MA, and accepted by the Editorial Board August 14, 2012 (received for review May 31, 2012)

Wind turbines convert kinetic to electrical energy, which returns to the atmosphere as heat to regenerate some potential and kinetic energy. As the number of wind turbines increases over large geographic regions, power extraction first increases linearly, but then converges to a saturation potential not identified previously from physical principles or turbine properties. These saturation potentials are >250 terawatts (TW) at 100 m globally, approximately 80 TW at 100 m over land plus coastal ocean outside Antarctica, and approximately 380 TW at 10 km in the jet streams. Thus, there is no fundamental barrier to obtaining half (approximately 5.75 TW) or several times the world's all-purpose power from wind in a 2030 clean-energy economy.

atmospheric modeling | climate feedbacks | renewable energy | water vapor | clean energy economy

A new method is proposed to determine the maximum theoretical wind power potential on Earth, based on the concept of "saturation". The *saturation wind power potential* (SWPP) is the maximum wind power that can be extracted upon increasing the number of wind turbines over a large geographic region, independent of societal, environmental, climatic, or economic considerations. Once the SWPP is reached, increasing the number of turbines further does not increase the generated power further. At the SWPP, winds still occur because individual turbines can extract no more than 59.3 % of the kinetic energy in the wind (Betz's limit). This paper also defines the *fixed wind power potential* (FWPP), which is the maximum power that can be extracted by a fixed number of wind turbines at decreasing installed density and increasing geographic area. The SWPP is calculated here at 100 m above ground, the hub height of most modern wind turbines, assuming conventional wind turbines distributed everywhere on Earth, including over the oceans (simulation named "global-SWPP") and, separately, over land only but excluding Antarctica ("land-SWPP"). The SWPP is also calculated at 10 km above ground in the jet streams assuming airborne wind energy devices ("jet stream-SWPP"). Capturing jet stream winds presents greater technological challenges than capturing surface winds but is still of interest (1, 2).

The main purpose of these simulations is to use a physical model to determine the theoretical limit of wind energy available at these altitudes, particularly because some recent studies that accounted for energy extraction by turbines, but not physically, have suggested that available wind energy is small (2, 3). Previous theoretical estimates of the power in the wind (4–9) are similarly not based on a physical model of energy extraction so cannot give estimates of wind potential at the height of turbines. As found here, energy extraction at a given altitude does not deplete energy at all altitudes above or below it; so an estimate of wind potential in the whole atmosphere does not answer the practical question about wind turbine potential at typical hub heights.

More relevant for practical applications, the FWPP of four million turbines at 100 m in three different configurations is quantified here to determine if this number is sufficient for powering half the world's all-purpose power demand in a 2030 clean-energy economy (10).

It is well known that the array efficiency of a single wind or water farm containing many turbines decreases with decreasing distance between turbines (11, 12). However, what is not known is the extent to which the efficiency loss operates globally when realistic meteorology and energy extraction by turbines are accounted for. This information is critical for determining the feasibility of a worldwide renewable energy future. Calculating the SWPP for large penetrations of wind (≥1 TW) is not currently possible from data analysis, because penetrations are still low (239 gigawatts (GW) installed worldwide at the start of 2012). The most accurate method available to analyze this issue is with a complex 3D atmospheric-ocean-land coupled model.

Previous global simulations of wind farms have assumed that wind farm effects on the atmosphere can be represented by changing surface roughness or adding a drag coefficient (2, 13–17). Roughness parameterizations, though, incorrectly reduce wind speeds the most in the bottom model layer, whereas in reality a surface wind turbine reduces wind speed the most at hub height, approximately 100 m above ground (Fig. 1). Because roughness lengths and drag coefficients are approximate, it is also difficult to ensure they extract the correct amount of energy from the wind. Calaf, et al. (18) demonstrated the inaccuracy of standard roughness parameterizations against large-eddy simulation results and developed a multiple layer roughness parameterization for ground-based turbines that is more accurate. Here, however, we use a straightforward approach to calculate the momentum sink at any specified hub height, not just near the ground, but also aloft, each time step, because it precisely determines the time-dependent energy extraction from one or many turbines.

Another common omission during modeling has been that of energy conservation during electric power use and turbulence dissipation. If wind turbines generate 5.75 TW (0.0113 W/m^2), such power ultimately returns to the air as heat following electricity use. This heat does not depend on the electricity source, thus it is also released when coal, nuclear, and natural gas produce electricity. Such generators, though, produce additional heat due to combustion or nuclear reaction and emit global warming pollutants (10, 19). As such, wind turbines reduce direct heat and pollutant emissions compared with conventional generators. However, the electricity use still needs to be accounted for because the heat is a source of some regenerated kinetic energy (via conversion of internal energy to some available potential energy to kinetic energy). To date, only ref. 1 has calculated the heat from electricity returned to the air, but they focused on airborne rather than ground-based wind turbines.

Author contributions: M.Z.J. and C.L.A. designed research; M.Z.J. and C.L.A. performed research; M.Z.J. contributed new reagents/analytic tools; M.Z.J. and C.L.A. analyzed data; and M.Z.J. and C.L.A. wrote the paper.

The authors declare no conflict of interest.

This article is a PNAS Direct Submission. M.B.M. is a guest editor invited by the Editorial Board.

[1]To whom correspondence may be addressed. E-mail: jacobson@stanford.edu or carcher@udel.edu.

This article contains supporting information online at www.pnas.org/lookup/suppl/doi:10.1073/pnas.1208993109/-/DCSupplemental.

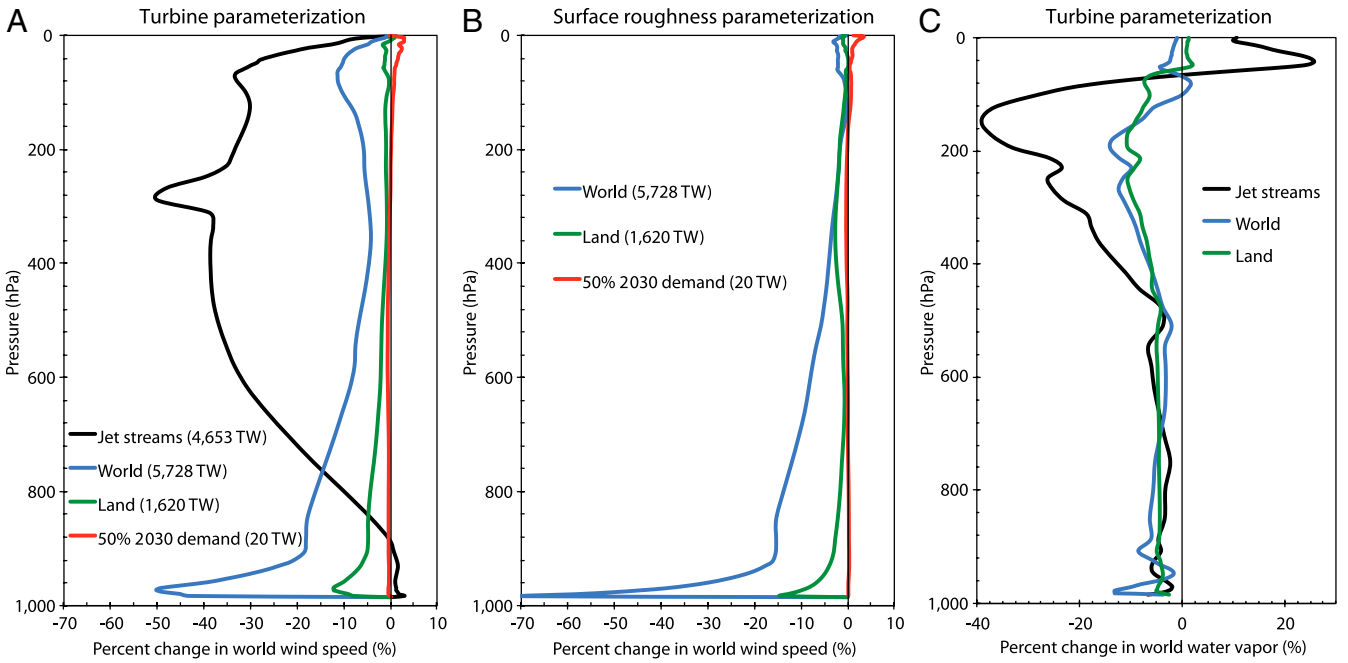

Fig. 1. Comparison of heights and magnitudes of globally averaged percent wind speed reduction averaged over one year from (*A*) the turbine momentum sink parameterization presented here vs. (*B*) the Lettau (33) surface roughness parameterizations. In both cases, the world is covered with either 1.146 billion (blue, world), 324.5 million (green, land), or four million (red, 50% of 2030 power demand) 5-MW, 126-m rotor diameter turbines with hub height of 100 m, spaced 0.44 km^2 each. A jet stream case is also shown in (*A*) for 931 million (black) 5-MW turbines with hub height at 10 km. (*C*) Percent difference in water vapor mass mixing ratio vertical profiles between the world (Simulation B), land (I), and jet stream (Q) cases and the base case (A). All these simulations were run at 4° × 5° horizontal resolution. Numbers in parentheses are installed wind power in each case, from Table 1.

Materials and Methods

Here, the GATOR-GCMOM global model (20, 21) is used to examine saturation and fixed wind power potentials. The model is modified to treat wind turbines as an elevated momentum sink, where the kinetic energy extracted from the wind is determined from a turbine power curve at the instantaneous model wind speed. The treatment of turbines developed is conceptually similar to that in (22, 23) but differs as follows: (*i*) it assumes each wind turbine occupies multiple vertical atmospheric layers rather than one layer, (*ii*) it is applied to numerous wind farms worldwide simultaneously rather than one local farm, (*iii*) it is applied in a global model where momentum extraction feeds back to global dynamics rather than a limited-area model with only regional feedbacks, and (*iv*) it accounts for energy conservation due to both electricity use and turbulent dissipation of kinetic energy. In addition, the new treatment allows distributed wind turbines in a grid cell to extract energy from four points on a staggered Arakawa C grid, thereby impacting five cells simultaneously, rather than from the center of the cell, affecting only that cell.

The *SI Materials and Methods* describes the model treatment of wind turbine kinetic energy extraction. Briefly, each turbine is characterized by a rated power [P_t, 5 megawatts (MW)], rotor diameter (D, 126 m), hub height above the topographical surface (H, 100 m or 10 km), and characteristic spacing area (A_t, m^2) each simulation. Each turbine is assumed to intersect multiple atmospheric layers of a grid column (Fig. S1). Each time step, kinetic energy is extracted from each model layer that intersects the turbine rotor. The kinetic energy reduction is translated into a wind speed reduction. The resulting shear produces turbulence that is combined with ambient mechanical and thermal turbulence. Energy is conserved by converting all electric power generated by the wind turbines to heat via electricity use at the surface, where it occurs, and by converting kinetic energy lost by natural surface roughness to turbulence, then heat.

Table 1 summarizes the simulations. A control simulation (A) was first run with turbines at 100 m hub height but no momentum extraction from them. In this case, the global capacity factor was about 31% based on instantaneous modeled wind speeds applied to the power curve for a 5-MW turbine with 126-m rotor diameter.

Fig. S2 compares resulting near-surface wind speeds with data. To determine the global-SWPP at 100 m, five 4° × 5° horizontal resolution sensitivity simulations (B–F) with momentum extraction, each with decreasing installed power density, were run. Simulations (G) (2.5° × 2.5°) and (H) (1.5° × 1.5°), comparable with (C), were then run to scale the coarse-resolution results to finer resolution.

To determine the land-SWPP (land excluding Antarctica) at 100 m, four 4°x5° simulations (I–L), each with decreasing power density, were run. A 1.5° × 1.5° simulation (M) was then run to scale results to finer resolution.

To determine the FWPP of four million 5-MW turbines, the number estimated to supply half the world's all-purpose power in a clean energy economy in 2030 (10), the turbines were distributed in three configurations: over all land 15S–60S and 15N–66.56N, and below 3 km altitude (Simulation N); over eight land and coastal sites (Table 1, footnote) (O); and over three land sites (Table 1, footnote) (P).

Finally, to determine the SWPP of the jet streams (10–70N and 10–70S) at 10 km, a 4° × 5° simulation (Q) with the maximum power density as in simulation (B) was run. A 1.5° × 1.5° simulation (R) was also run to scale results with resolution.

All simulations included 68 vertical sigma-pressure layers up to 0.219 hPa (≈60 km), including 15 layers from 0–1 km and 500-m resolution from 1–21 km. The center of the lowest model layer was 15 m above ground. The rotor of each surface turbine (simulations B–P) intersected five model layers. That of each jet-stream turbine (simulations Q–R) intersected two layers. The model was run forward from January 1, 2006 with no data assimilation. Because this study does not focus on temperature response and due to the long computer time required for radiative, cloud, aerosol, and gas processes, only five-year simulations were run. Wind power extraction in all five years was similar and convergent in all simulations.

Results

Fig. 2*A* shows that, up to about 715 TW (1.4 W/m^2) of installed power, the output from power-extracting wind turbines first increases linearly. The linearity is demonstrated by comparing the initial slope of the "global-SWPP curve" (with power extraction) with the slope of the "global-no power extraction" line. The latter is the line between zero and the power output from Simulation A, which is the reference case with turbines but without power extraction. At higher penetrations, power output increases with diminishing returns until it reaches global saturation (approximately 253 TW, also Fig. S3*B* for coarse-resolution results) at about 2,870 TW (5.65 W/m^2) installed. Higher penetrations of wind serve no additional benefit. Thus, for the first 715 TW

Table 1. Summary of simulations and power output in year 5

Simulation	Model horizontal resolution (degrees)	Turbine spacing A_t (m^2)	Total number of 5-MW turbines (millions)	Number of turbines over ocean (millions)	Total installed power (TW)	Percent of world for spacing	Turbine installed power density (W/m^2)	Annual total power output year 5 (TW)
Global-SWPP								
A) World (control)	4 × 5	$28D^2$	1,146	821	5,730	100	11.3	1,750
B) World	4 × 5	$28D^2$	1,146	821	5,730	100	11.3	224
C) World	4 × 5	$56D^2$	573	411	2,864	100	5.62	228
D) World	4 × 5	$84D^2$	382	274	1,909	100	3.75	219
E) World	4 × 5	$112D^2$	286	205	1,432	100	2.81	206
F) World	4 × 5	$224D^2$	143	103	716	100	1.41	160
G) World	2 × 2.5	$56D^2$	574	410	2,870	100	5.65	251*
H) World	1.5 × 1.5	$56D^2$	575	410	2,872	100	5.65	**253***
Land-SWPP[†]								
I) Land	4 × 5	$28D^2$	299	0	1,495	26.0	11.3	71.2
J) Land	4 × 5	$56D^2$	149	0	747.6	26.0	5.62	66.7
K) Land	4 × 5	$112D^2$	74.8	0	373.8	26.0	2.81	56.4
L) Land	4 × 5	$224D^2$	37.4	0	186.9	26.0	1.41	39.7
M) Land	1.5 × 1.5	$28D^2$	302	0	1,510	26.3	11.3	**72.0***
Land-FWPP								
N) Land[‡]	4 × 5	$1{,}470D^2$	4	0	20	18.3	0.21	**7.50**
O) Land+coast 8 sites[§]	4 × 5	$56D^2$	4	0.004	20.195	0.696	5.62	**3.93**
P) Land 3 sites[¶]	4 × 5	$28D^2$	4	0	20.105	0.348	11.3	**1.63**
Jet stream-SWPP								
Q)Jet stream[‖]	4 × 5	$28D^2$	931	668	4,653	81.0	11.3	375
R) Jet stream[‖]	1.5 × 1.5	$28D^2$	941	673	4,707	81.9	11.3	**378***

Earth's surface area is 510.6 million km^2. Hub heights were 100 m above ground level except in the jet stream cases (10 km). $D = 126$ m is turbine rotor diameter.

*The 1.5° × 1.5° simulations were run for only six months and the 2° × 2.5° simulations, for one year, due to their enormous computing requirements. The ratio of the power generation averaged over the months or year to that from the same time for the corresponding 4° × 5° resolution simulation was multiplied by the last-year annual-average result from the 4° × 5° simulation to estimate the 1.5° × 1.5° and 2° × 2.5° power generation averaged over the last year for conditions from that simulation.

[†]Land in these cases included all land north of 60S (outside of Antarctica) but did not include coastal ocean.

[‡]Land in this case included all land 15S–60S and 15N–66.56083N (Arctic Circle), and below 3 km altitude but did not include coastal ocean.

[§]All turbines in this case were distributed among 19 windy cells in 8 locations: the Great Plains (4 cells), offshore East Coast (3), the North Sea (2), the Sahara Desert (3), the Gobi Desert (2), the Yellow Sea (1), Australia (2), and Patagonia (2).

[¶]All turbines in this case were distributed among nine windy cells in three locations: the Great Plains (4 cells), the Sahara Desert (3), and the Gobi Desert (2).

[‖]The jet stream winds considered were 10S–70S and 10N–70N, and at 10 km altitude. Top and bottom turbine heights were 10.063 km and 9.937 km, respectively.

installed, output increases roughly linearly proportionally to turbine installation, but thereafter, it increases with diminishing returns until saturation.

The global SWPP obtained in Fig. 2*A* is likely a lower bound because power extraction increases, while still converging, upon grid refinement. For example, 1.5° × 1.5° resolution results (Simulation H) were about 1% higher than those at 2° × 2.5° (Simulation G), which were about 10% higher than at 4° × 5° (Simulation C). Even higher resolution may increase power output more (24).

The 253 TW of worldwide extractable power at 100 m is approximately 22.5 times that of a previous simple-equation estimate of extractable power in the bottom 200 m of the atmosphere worldwide (11.25 TW) calculated by ref. 3 as the estimated

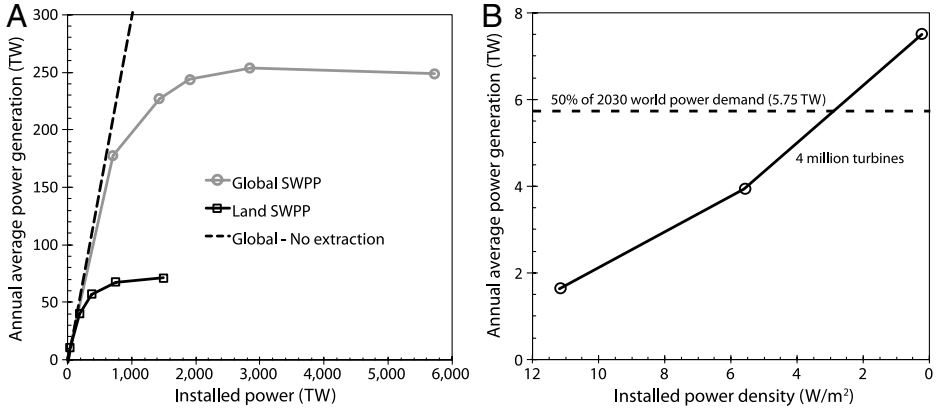

Fig. 2. (*A*) Convergence to global-SWPP (Simulations B–F) and land-SWPP outside Antarctica (Simulations I–L and N) scaled by higher-resolution results from Simulations H and M, respectively. As such, values represent 4° × 5° results from Table 1 scaled by 1.5° × 1.5° results, from the table. Also shown is the straight line between 0 and 1,750 TW power output (at 5,730 TW, or 11.3 W/m^2, installed power) from the global turbine, no-power-extraction case (Simulation A). The highest installed turbine density in the land-SWPP case was also 11.3 W/m^2. (*B*) Wind power potential at three installed power densities of four million wind turbines. Also shown is 50% of the world all-purpose power demand in 2030 upon conversion to wind, water, and sunlight (WWS) and electricity/electrolytic hydrogen.

total power in that region (100 TW) multiplied by the fraction that could interact with wind turbine rotors (<0.3), the fraction in the range of turbine cut-in and cut-out speeds (0.75), and the fraction converted from kinetic to electrical energy (0.5). These factors were all accounted for in time and space in the simulations here. The large difference highlights the importance of using physical calculations.

The SWPP over land outside Antarctica here was approximately 72 TW (Fig. 2*A* and Fig. S3*C*). Based on the high-resolution global-SWPP calculations here, another approximately 8 TW was available offshore at depths <200 m, giving a land plus coastal SWPP estimate of 80 TW. Like with the global case, the land-SWPP curve (Fig. 2*A*) shows a linear portion at low turbine penetrations. Beyond approximately 185 TW of installed power, diminishing returns set in. However, the full land-SWPP was not obtained until approximately 1,500 TW (11.3 W/m^2) of installed power. The result here suggests that bottom-up approaches for calculating wind power potentials over land are justified for <185 TW installed power.

The land-SWPP is not much lower than the 125 TW of onshore power from a study (25) that assumed a fixed percentage energy loss due to turbine interference but not increasing competition for wind with increasing turbine penetration. Results from (25) fall near the linear "global-no extraction" curve in Fig. 2*A*, just above the land-SWPP.

Another study (26) estimated the world land plus coastal wind potential based on world sounding and surface data as 72 TW. Similarly, ref. 25 estimated a land potential of 78 TW for capacity factors of 20% or higher. Both studies accounted only for locations with mean-annual wind speeds before extraction >7 m/s and did not account for increasing competition. These two offsetting factors caused their results to be similar to the land-SWPP (72 TW) and the land plus near-shore estimate (approximately 80 TW) found here.

If only 50% of land-based wind were in economically viable locations (3), the feasible wind potential on land (not counting near shore) here would be approximately 36 TW, 36 times the single-equation estimate from ref. 3.

The SWPP at 10 km in the jet streams (approximately 378 TW—Table 1 and Fig. S3*G*) was approximately 150% that at 100 m despite fewer turbines in the jet stream case. The maximum jet stream power availability was approximately 50 times that of a 7.5 TW estimate from ref. 2, who used a global model with only 10 vertical layers to minimize computer time (vs. 68 layers here) and an elevated drag coefficient rather than extracting momentum based on a turbine power curve. The difference again highlights the importance of calculating the SWPP from physical principles. SWPPs are extractable energy potentials, not just available energy potentials, thus include losses and efficiencies. Airborne jet-stream turbines would require energy to ascend and descend and may not operate all year. This analysis does not quantify such losses, only extractable energy.

The extractable power globally at 100 m and, separately, at 10 km in the jet streams, are both independently less than the total extractable power in the wind at all altitudes, estimated broadly as 450–3,800 TW (4–9). These previous studies, though, did not consider extraction at a single altitude, such as the height of modern wind turbines nor did they use a 3D model to make their estimates. Extraction of power at each 100 m and at 10 km does not give the same dissipation as complete extraction of kinetic energy from the atmosphere, as seen in Fig. 1; instead, each results in wind reduction over a vertical segment of the atmosphere, decreasing with distance from the height of extraction.

Simulations N-P examine whether approximately four million 5-MW turbines (20 TW installed) can provide at least 5.75 TW of delivered power, enough to supply 50% of all-purpose end-use power demand in 2030 for a world energy infrastructure converted to wind, water, and sunlight (WWS) and electricity/hydrogen (10). Fig. 2*B* shows that the power output of four million turbines increases with decreasing wind turbine spacing. When turbines are packed at an installed density of 11.3 W/m^2 into three sites worldwide, the power output is too low (approximately 1.6 TW—Table 1 and Fig. S3*F*) to match power demand. At eight locations (5.6 W/m^2 installed), the output improves to approximately 4 TW (Fig. S3*E*) but is still lower than needed. However, when turbines are spread over land outside the tropics, away from the poles, and in all regions below 3 km altitude (0.11 W/m^2 installed), the output jumps to approximately 7.5 TW (Fig. S3*D*), much more than needed. The crossover point is at an installed density of approximately 2.9 W/m^2. It is not necessary to spread turbines evenly across such land. In fact, individual farms can have installed densities of 5.6–11.3 W/m^2 so long as reasonable spreading between farms occurs and the average installed density within and between farms is ≤2.9 W/m^2 (or ≤3.1 W/m^2 accounting for higher model resolution).

Discussion

It is well known that spreading wind turbines in a farm increases farm array efficiency by decreasing interference of one turbine with the next (11, 12). The results here suggest that staggering farms themselves, geographically, improves the overall power output. In other words, the power potential of a fixed number of turbines (FWPP) increases with increased spreading of farms.

The addition of surface wind turbines reduced horizontal wind speeds in their wake the most and below and above the wake centerline to a lesser extent (Fig. 1*A*). The reduction in wake wind speed reduced shearing stress below and increased it above the wake centerline, consistent with large-eddy-simulation results (18). Greater shearing stress above the wake increased subgrid-scale turbulent kinetic energy (TKE) there, increasing the downward transport of horizontal momentum from above to the turbines. Downward transport of horizontal momentum to a turbine wake was also increased in the model by subgrid-scale thermal turbulence and grid-scale gravity waves when they were present. Lesser shearing stress below the wake decreased TKE and downward momentum fluxes near the surface, as in ref. 18. Evaporation rates are proportional to both surface wind speed and surface shearing stress, and both decreased in all surface turbine simulations, reducing evaporation and water vapor (e.g., Fig. 1*C*). These calculations were all made with the model resolving the bottom kilometer with 15 vertical layers, including five layers intersecting turbine rotors.

Drag from blade rotation also creates turbulence in the form of small-scale vortices that can enhance mixing. This mechanism has been suggested by ref. 27 to explain why wind turbines decrease downwind surface temperatures during the day, when the lapse rate is generally unstable, and slightly increase them at night, when the lapse rate is generally stable but winds at hub height are stronger. However, blade-generated turbulence under neutral conditions is observed to be transported and dissipate downwind in a spiral motion (28), with greater turbulence intensity above the turbine centerline than below (28, 29). While such turbulence reduces mean wind speeds in the wake, it also increases the downward transport of faster winds from aloft into the wake. Blade-generated turbulence is transported vertically due to shear turbulence generated by the velocity deficit in the wake and ambient turbulence rather than on its own (28). As such, blade-generated turbulence decreases substantially between its peak above the centerline and surface and little may get to the surface, as indicated by at least some measurements and high-resolution modeling (figure 1 of ref. 29). This result may differ under very unstable conditions. Even when blade-generated turbulence reaches the ground, it may largely be offset by reduced shearing stress below the turbine caused by reduced wind speed in the wake, resulting in little net surface turbulence, consistent with the aforementioned measurements (29). Both the reduced wind

speed and small turbulence change near the surface due to turbines contributed in the model to reducing surface evaporation. Uncertainties in the treatment of turbulence still exist due to both the coarse horizontal resolution of the model and the simplification of no turbine-rotor generated turbulence.

Reduced evaporation reduced evaporative cooling of the surface, first warming the surface. However, because evaporated water vapor normally recondenses in the atmosphere to form clouds, releasing latent heat there, the reduction in water vapor reduced latent heat release in the air, cooling the air due as a result of this process. Because water vapor contributes to air pressure, reducing water vapor also reduced globally averaged air pressure by approximately 0.3 and approximately 0.1 hPa in the global (Simulation B) and land (I) cases, respectively. Because water vapor is a greenhouse gas, reducing it increased thermal-IR radiation escape to space, cooling the surface further. However, less water also reduced cloudiness, increasing solar radiation to the surface during the day but increasing outgoing thermal-IR at night, thus causing a slight warming at night, as observed (27, 30). The net effect of all five changes (air cooling due to lower atmospheric latent heat release, ground warming due to lower surface water evaporation, air and ground cooling due to a reduced water vapor greenhouse effect, ground warming due to reduced daytime cloudiness, and ground cooling due to reduced nighttime cloudiness) was a globally averaged surface-air temperature decrease in 15 out of the 16 surface-turbine simulations. This result is expected because water vapor is known to cause net warming of the atmosphere, so reducing it should cause cooling (31). Temperature results, though, are still uncertain, particularly due to the uncertainty of clouds and the transient nature of the simulations and could change over longer simulations because full temperature responses take decades to realize. A certain benefit of the slower winds, though, is the reduction in wind-driven soil dust; sea spray; and spore, pollen, and bacteria emissions, reducing human exposure to small particles that penetrate deep into the lungs.

Globally distributed turbines decreased zonal winds; however, they increased meridional winds in the pole-ward direction in both hemispheres (Fig. S4 *A* and *B*). The pole-ward transport of air increased the pressure gradient between the poles and Equator by approximately 15–25 hPa, supporting the contention that the atmosphere responded to the increased dissipation of kinetic energy by increasing some of its available potential energy via enhanced pole-to-Equator pressure gradients. Reduced water vapor partial pressure at low latitudes contributed slightly to the enhanced pressure gradient.

Global warming increases temperatures at the poles more than lower latitudes. The temperature gradient reduction could reduce global near-surface wind resources in the future although ocean wind resources over the last 25 years have increased in the global average according to multiple datasets (32). Higher water vapor due to future warming will also likely offset reduced water vapor due to wind turbines.

Jet-stream turbines reduced mean wind speeds at altitudes above and below them, but increased boundary-layer wind speeds (Fig. 1*C*). Like in the surface case, turbines decreased zonal wind speeds substantially (Fig. S5*A*), but increased meridional wind speeds (Fig. S5*B*), moving air pole-ward at 10 km but equator-ward near the surface in both hemispheres, following the respective pressure gradients (Fig. S5*C*). Lower surface pressure in the tropics through midlatitudes caused air to rise, expand, and cool adiabatically, decreasing temperatures at all altitudes (Fig. S5*D*) and increasing both cloud liquid below 5 km (Fig. S5*E*) and cloud ice above that. Enhanced cloudiness increased precipitation, and both, together with net divergence, decreased water vapor in the tropics and subtropics and increased it toward the poles (Fig. S5*F*). Compressional heating over the poles increased temperatures there, but the net effect of jet stream turbines was surface cooling by >1 K (Fig. S5*F*), as cold air advection from the Poles prevailed near the surface. Interestingly, the higher boundary-layer wind speeds (Fig. 1*C* and Fig. S5*A*) increased evaporation there, but enhanced condensation of that vapor decreased column vapor at low latitudes (Fig. S5*F*).

In sum, increasing the number of wind turbines worldwide allows energy extraction relatively proportional to the number of turbines until saturation is reached. Saturation occurs when sources of kinetic energy at nearby altitudes and creation of kinetic from potential energy are exhausted. At saturation, each additional turbine still extracts energy, but that extraction reduces energy available to other turbines, so the average extraction among all turbines decreases to maintain a constant SWPP. The results here suggest that saturation of wind power availability will not limit a clean-energy economy. However, spreading wind farms out worldwide in high-wind locations will increase wind farm efficiency and reduce the number of farms needed compared with packing wind farms side-by-side. The careful siting of wind farms will minimize costs and the overall impacts of a global wind infrastructure on the environment.

ACKNOWLEDGMENTS. Funding sources include National Science Foundation, U.S. Environmental Protection Agency, and National Aeronautics and Space Administration high-end computing.

1. Archer CL, Caldeira K (2009) Global assessment of high-altitude wind power. *Energies* 2:307–319.
2. Miller LM, Gans F, Kleidon A (2011) Jet stream wind power as a renewable energy resources: Little power, big impacts. *Earth Syst Dynam* 2:201–212.
3. De Castro C, Mediavilla M, Miguel LJ, Frechoso F (2011) Global wind power potential and technological limits. *Energy Policy* 39:6677–6682.
4. Lorenz EN (1967) *The Nature and Theory of the General Circulation of the Atmosphere* (WMO, Geneva) p 161.
5. Gustavson MR (1979) Limits to wind power utilization. *Science* 204:13–17.
6. Peixoto JP, Oort AH (1992) *Physics of Climate* (American Institute of Physics, New York) p 520.
7. Sorensen B (2004) *Renewable Energy: Its Physics, Engineering, Use, Environmental Impacts, Economy, and Planning Aspects* (Elsevier Academic Press, London), 3rd Ed, p 86.
8. Li L, Ingersoll AP, Jiang X, Feldman D, Yung YL (2007) Lorenz energy cycle of the global atmosphere based on reanalysis datasets. *Geophys Res Lett* 34:L16813.
9. Stacey FD, Davis PM (2008) *Physics of the Earth* (Cambridge Univ Press, Cambridge), 4th Ed, p 531.
10. Jacobson MZ, Delucchi MA (2011) Providing all global energy with wind, water, and solar power, part I: Technologies, energy resources, quantities and areas of infrastructure, and materials. *Energy Policy* 39:1154–1169.
11. Milborrow DJ (1980) The performance of arrays of wind turbines. *J Wind Eng Ind Aerod* 5:403–430.
12. Li Y, Calisal SM (2010) Estimating power output from a tidal current turbine farm with first-order approximation of hydrodynamic interaction between turbines. *Int J Green Energy* 7:153–163.
13. Keith DW, et al. (2004) The influence of large-scale wind power on global climate. *Proc Natl Acad Sci USA* 101:16115–16120.
14. Kirk-Davidoff DB, Keith D (2008) On the climate impact of surface roughness anomalies. *J Atmos Sci* 85:2215–2234.
15. Barrie D, Kirk-Davidoff DB (2010) Weather response to a large wind turbine array. *Atmos Chem Phys* 10:769–775.
16. Wang C, Prinn RJ (2010) Potential climatic impacts and reliability of very large-scale wind farms. *Atmos Chem Phys* 10:2053–2061.
17. Miller LM, Gans F, Kleidon A (2011) Estimating maximum global land surface wind power extractability and associated climatic consequences. *Earth Syst Dynam* 2:1–12.
18. Calaf M, Meneyeau C, Meyers J (2010) Large eddy simulation study of fully developed wind-turbine array boundary layers. *Phys Fluids* 22:015110.
19. Sta Maria MRV, Jacobson MZ (2009) Investigating the effect of large wind farms on energy in the atmosphere. *Energies* 2:816–836.
20. Jacobson MZ, Wilkerson JT, Naiman AD, Lele SK (2011) The effects of aircraft on climate and pollution. Part I: Numerical methods for treating the subgrid evolution of discrete size- and composition-resolved contrails from all commercial flights worldwide. *J Comp Phys* 230:5115–5132.
21. Jacobson MZ, Ten Hoeve JE (2012) Effects of urban surfaces and white roofs on global and regional climate. *J Climate* 25:1028–1044.
22. Baidya Roy S, Pacala SW, Walko RI (2004) Can large wind farms affect local meteorology. *J Geophys Res* 109:D19101.
23. Baidya Roy S (2011) Simulating impacts of wind farms on local hydrometeorology. *J Wind Eng Ind Aerod* 99:491–498.

24. Pryor SC, Nikulin G, Jones C (2012) Assessing climate change impacts on the near-term stability of the wind energy resources over the United States. *J Geophys Res* 117:D03117.
25. Lu X, McElroy M, Kiviluoma J (2009) Global potential for wind-generated electricity. *Proc Natl Acad Sci USA* 106:10933–10938.
26. Archer CL, Jacobson MZ (2005) Evaluation of global wind power. *J Geophys Res* 110:D12110.
27. Zhou L, et al. (2012) Impacts of wind farms on land surface temperatures. *Nature Climate Change* 2:539–543.
28. Vermeer LJ, Sorensen JN, Crespo A (2003) Wind turbine wake aerodynamics. *Progr Aero Sci* 39:467–510.
29. Crespo A, Hernandez J (1996) Turbulence characteristics in wind-turbine wakes. *J Wind Eng Ind Aerod* 61:71–85.
30. Baidya Roy S, Traiteur JJ (2010) Impacts of wind farms on surface air temperatures. *Proc Natl Acad Sci USA* 107:17899–17904.
31. Kiehl JT, Trenberth KE (1997) Earth's annual global mean energy budget. *Bull Am Meteorol Soc* 78:197–208.
32. Wentz FJ, Ricciardulli L (2011) Comment on "Global trends in wind speed and wave height". *Science* 334:905.
33. Lettau H (1969) Note on aerodynamic roughness-parameter estimation on the basis of roughness-element description. *J Appl Meteorol* 8:828–832.

Supporting Information

Jacobson and Archer 10.1073/pnas.1208993109

SI Text

SI Materials and Methods. The model used for this study was GATOR-GCMOM, a global-through-urban nested model (1–3). The model was modified to treat wind turbines as an elevated sink of momentum, where the kinetic energy extracted from the wind is determined from a turbine power curve at the instantaneous model wind speed. The treatment of turbines developed here is similar in concept to that of *Baidya Roy* (4, 5) but differs in the following ways: it (*i*) assumes each wind turbine occupies multiple vertical atmospheric layers rather than one layer, (*ii*) is applied to numerous wind farms worldwide simultaneously rather than one local farm, (*iii*) is applied in a global model where momentum extraction feeds back to global dynamics rather than a limited-area model with only regional feedbacks, and (*iv*) accounts for the conservation of energy due to both electricity use and turbulent dissipation of kinetic energy. In addition, the new treatment allows distributed wind turbines in a grid cell to extract energy from a staggered Arakawa C grid rather than from the center of the cell. With the C grid, u, and v are located at grid cell edges. As such, turbines distributed throughout a grid cell alter wind speeds at four locations in the cell rather than at one central location. Because cell edges join two cells, wind speed changes with the C grid affect five cells simultaneously rather than one.

The treatment of kinetic energy extraction by wind turbines in the model is described as follows. Each turbine is characterized by a rated power [P_t, 5 megawatts (MW)], a rotor diameter (D, 126 m), a hub height above the topographical surface (H, 100 m), and a characteristic spacing area (m^2) $A_t = xD \times yD$, usually determined by convention to minimize interference of the wake of one turbine with the next turbine. In this equation, x and y are constants that provide distances perpendicular to and parallel to, respectively, the prevailing wind direction. Some values used previously have been $x = 4$, $y = 7$; $x = 3$, $y = 10$ (6).

Each model grid cell contains a specified number of turbines. The maximum number of turbines in the grid cell is $N_t = A_c/A_t$, where A_c is the ground area occupied by the cell (m^2).

For determining extraction of energy, each turbine is assumed to intersect one or more atmospheric layers of a grid column. This configuration applies regardless of whether the turbines exist in the boundary layer or jet stream and for either global or regional domains. The configuration requires modification only when the horizontal resolution of the model $< D (= 126$ m in the present application). All simulations here were run at coarser horizontal resolution than this resolution.

The momentum extracted from each layer k that the turbine intersects is proportional to the ratio of the swept area of the turbine residing in the layer (S_k) divided by the total swept area (m^2) of the turbine, $S_t = \pi D^2/4$. The swept area residing in a layer is determined from geometry. For example, the swept area falling in the lowest layer of Fig. S1 (ABCDA) is the area HADCH minus the area HABCH. Because the hub height (point H) and the height above the ground of the edge of each layer (e.g., point B) are known, the vertical distance HB is also known. Because the distance HC, which is the turbine radius $R = D/2$, is also known, the angle BHC is $\theta_{\text{BHC}} = \arccos(\text{HB}/R)$. Therefore, area $\text{HADCH} = 2\theta_{\text{BHC}} S_t/2\pi$, and area $\text{HABCH} = \text{HB} \times R\sin(\theta_{\text{BHC}})$. The areas of subsequent layers are calculated from bottom to top in a similar manner, taking into account the summed areas determined already.

Kinetic energy is extracted from each model layer that intersects the turbine rotor each time step Δt due to conversion of the kinetic energy to electric power by the turbine. The global and regional domains in the model use the Arakawa C grid structure; thus, u scalar velocities are located at the west $(i - 1/2, j)$ and east $(i + 1/2, j)$ edges of each grid cell in each layer k, v scalar velocities are located at the south $(i, j - 1/2)$ and north $(i, j + 1/2)$ edges, and mass M (kg) and other scalars are located at the center (i, j, k) of the cell. As such, the initial (subscript I) total kinetic energy in grid cell i, j, k before energy extraction is

$$E_{\text{I},i,j,k} = 0.5(E_{\text{I},i-1/2,j,k} + E_{\text{I},i+1/2,j,k} + E_{\text{I},i,j-1/2,j,k} + E_{\text{I},i,j+1/2,j,k}). \quad \textbf{[S1]}$$

In this equation,

$$\begin{aligned}
&E_{\text{I},i-1/2,j,k} = 0.5 M_{i-1/2,j,k} u^2_{\text{I},i-1/2,j,k},\\
&\quad \text{where } M_{i-1/2,j,k} = 0.5(M_{i-1,j,k} + M_{i,j,k})\\
&E_{\text{I},i+1/2,j,k} = 0.5 M_{i+1/2,j,k} u^2_{\text{I},i+1/2,j,k},\\
&\quad \text{where } M_{i+1/2,j,k} = 0.5(M_{i,j,k} + M_{i+1,j,k})\\
&E_{\text{I},i,j-1/2,k} = 0.5 M_{i,j-1/2,k} v^2_{\text{I},i,j-1/2,k},\\
&\quad \text{where } M_{i,j-1/2,k} = 0.5(M_{i,j-1,k} + M_{i,j,k})\\
&E_{\text{I},i,j+1/2,k} = 0.5 M_{i,j+1/2,,k} v^2_{\text{I},i,j+1/2,,k},\\
&\quad \text{where } M_{i,j+1/2,k} = 0.5(M_{i,j,k} + M_{i,j+1,k}). \quad \textbf{[S2]}
\end{aligned}$$

The average horizontal wind speed at the vertical and horizontal center of a cell, used to determine kinetic energy extraction by a wind turbine to produce electricity, is thus $W_{i,j,k} = [2E_{\text{I},i,j,k}/M_{i,j,k}]^{1/2}$. Each time step, the kinetic energy extracted from the turbine in a given cell is calculated as

$$\Delta E_{i,j,k} = P_{i,j,k} \Delta t S_k / S_t, \quad \textbf{[S3]}$$

where $P_{i,j,k}$ is the power extracted from the turbine at instantaneous wind speed $W_{i,j,k}$ based on its power curve. Eq. **S3** implies that the power determined from the power curve is calculated with a different wind speed in each model layer intersecting the turbine. Whereas power curves are derived based on the wind speed at hub height, the assumption of varying power extraction for varying heights in the turbine is necessary, because otherwise it would be possible to extract more energy from a layer than is physically present. For example, suppose (in a hypothetical extreme case), the wind speed were 0 m/s in the lowest layer intersecting the turbine and 10 m/s at hub height. Subtracting a portion of the total energy extracted from the lowest layer would be unphysical. Because wind speeds vary roughly logarithmically with height and the height of a turbine swept area is only D, higher wind power extracted at the turbine top are roughly compensated for by lower power extracted at the bottom. The error due to this assumption is likely less than the error due to that of the power curve, which is derived under neutrally stratified conditions in the absence of wind shear.

For the REPower 5-MW turbine, a fit to the power curve data, combined with a correction for air density, is

$$P_{i,j,k} = \frac{\rho_a(T,P,q)}{\rho_{a,\mathrm{STP}}} \begin{cases} 0 & W_{i,j,k} < 3.5002 \text{ m/s} \quad \text{or} \quad W_{i,j,k} > 30 \text{ m/s} \\ 807.69 + W_{i,j,k}(-495.51 + W_{i,j,k}(77.88 - 0.64 W_{i,j,k})) & 3.5002 \le W_{i,j,k} \le 10 \text{ m/s} \\ 12,800 + W_{i,j,k}(-5713.3 + W_{i,j,k}(740.0 - 26.667 W_{i,j,k})) & 10 < W_{i,j,k} \le 13 \text{ m/s} \\ 5000 & 13 < W_{i,j,k} \le 30 \text{ m/s} \end{cases} \quad \textbf{[S4]}$$

based on manufacturer-provided power output vs. wind speed, where $\rho_{a,\mathrm{STP}} = 1.225$ kg/m^3 is air density at standard temperature and pressure and $\rho_a(T,P,q)$ is air density at the current temperature (T), pressure (P), and specific humidity (q) in the model. The power curve indicates a cut-in wind speed of 3.5 m/s, a cut-out wind speed of 30 m/s, and a rated wind speed of 13 m/s.

The final kinetic energy in each grid cell is thus $E_{\mathrm{F},i,j,k} = E_{\mathrm{I},i,j,k} - \Delta E_{i,j,k}$. The turbine also converts some kinetic energy into turbulent kinetic energy (TKE), primarily in the vertical. This conversion is roughly accounted for in the model because the reduction in wind speed due to the turbine results in wind shear, creating subgrid-scale mechanical turbulence and TKE through a level 2.5 TKE closure scheme (7). The increase in TKE increases the turbulent diffusion coefficient for momentum, increasing the vertical transport of horizontal momentum down gradients (and reducing it up gradients) in the presence of the turbine-generated turbulence or large-scale shear- or buoyancy-driven turbulence in a second-order local closure diffusion calculation in the model. Energy, moisture, and trace chemicals are similarly transported across gradients due to turbulent diffusion. No treatment of constructive or destructive interference by wakes is introduced because wakes are not resolved at the scale of interest.

The change in total kinetic energy in the grid cell is next partitioned proportionately among the kinetic energies of the surrounding u and v points with

$$\begin{aligned} E_{\mathrm{F},i-1/2,j,k} &= E_{\mathrm{I},i-1/2,j,k} E_{\mathrm{F},i,j,k} / E_{\mathrm{I},i,j,k} \\ E_{\mathrm{F},i+1/2,j,k} &= E_{\mathrm{I},i+1/2,j,k} E_{\mathrm{F},i,j,k} / E_{\mathrm{I},i,j,k} \\ E_{\mathrm{F},i,j-1/2,k} &= E_{\mathrm{I},i,j-1/2,,k} E_{\mathrm{F},i,j,k} / E_{\mathrm{I},i,j,k} \\ E_{\mathrm{F},i,j+1/2,k} &= E_{\mathrm{I},i,j+1/2,,k} E_{\mathrm{F},i,j,k} / E_{\mathrm{I},i,j,k}. \end{aligned} \quad \textbf{[S5]}$$

The final wind speed at each u and v point is then

$$\begin{aligned} u_{\mathrm{F},i-1/2,j,k} &= \mathrm{sign}\left(\sqrt{2E_{\mathrm{F},i-1/2,j,k}/M_{i-1/2,j,k}}, u_{\mathrm{I},i-1/2,j,k}\right) \\ u_{\mathrm{F},i+1/2,j,k} &= \mathrm{sign}\left(\sqrt{2E_{\mathrm{F},i+1/2,j,k}/M_{i+1/2,j,k}}, u_{\mathrm{I},i+1/2,j,k}\right) \\ v_{\mathrm{F},i,j-1/2,k} &= \mathrm{sign}\left(\sqrt{2E_{\mathrm{F},i,j-1/2,k}/M_{i,j-1/2,k}} v_{\mathrm{I},i-1/2,j,k}\right) \\ v_{\mathrm{F},i,j+1/2,k} &= \mathrm{sign}\left(\sqrt{2E_{\mathrm{F},i,j+1/2,k}/M_{i,j+1/2,k}} v_{\mathrm{I},i+1/2,j,k}\right), \end{aligned} \quad \textbf{[S6]}$$

where sign() indicates that the sign of the final scalar velocity needs to be that of the initial value. Because each u and v point borders two grid cells, it is necessary to ensure that all grid cells are solved independently with initial wind speeds and that final u and v wind speeds at each border point are determined by adding differences from Eq. **S6**, such as $u_{\mathrm{F},i-1/2,j,k} - u_{\mathrm{I},i-1/2,j,k,}$ for both adjacent cells to the initial value, $u_{\mathrm{I},i-1/2,j,k}$, to obtain the final wind speed at the border point.

Energy conservation due to power generation and frictional dissipation of winds at the surface is maintained in the model by converting all electric power generated by the wind turbines to heat. The model also converts kinetic energy lost by natural surface roughness to turbulence and then heat. The electric power generated by turbines each time step, $\Delta E_{i,j,k}$, modifies the surface air temperature (where the electric power is consumed by human activity). Because the global model grid cells for the present simulations are large, it is assumed that the electricity is consumed in the same column that it is generated in. The temperature change (K) during a time step in surface layer *ksfc* due to electric power extraction in the model layers k between the bottom and top of a turbine rotor is

$$\Delta T_{i,j,ksfc} = \frac{1}{c_{p,m} M_{i,j,ksfc}} \sum_{k=\mathrm{bottom}}^{\mathrm{top}} \Delta E_{i,j,k}, \quad \textbf{[S7]}$$

where $c_{p,m}$ is the specific heat of moist air at constant pressure. Similarly the u- and v-components of kinetic energy lost due to friction and TKE generation at the topographical surface each time step are converted to internal energy and added to the temperature in the bottom model layer.

The model was initialized with $1° \times 1°$ reanalysis meteorological fields (8) for simulations starting January 1, 2006 and run forward in time for five years with no data assimilation, as described in the main text. Oceans in the model were represented in 3D for some calculations and 2D for others. A 2D time-dependent mixed-layer ocean dynamics model driven by surface wind stress was used to solve for mixed-layer velocities, heights, and horizontal energy transport in each grid cell (9). The scheme conserves potential enstrophy, vorticity, energy, and mass and predicts gyres and major currents. Energy diffusion to the deep ocean was treated in 3D through 10 ocean layers below each surface grid cell. Air-ocean exchange, vertical diffusion through the ocean, and 3D ocean equilibrium chemistry and pH were solved as in (10).

Sea ice in the model could form on water surfaces, and snow could accumulate on sea ice. The model solved for the temperature at the ice-ocean interface, the snow-ice interface, the air-snow interface, and the air-ice interface as in (1), which assumed single layers of sea ice and snow on top of sea ice whose thicknesses were solved for over time. When the weight of sea ice plus snow caused the sea ice to submerge below sea level, snow was converted to sea ice. Although snow on top of sea ice was treated as one layer, the vertical density profile in the layer was calculated and other properties of snow varied with density. For permanent snow over land, the 10-layer subsurface model was used to transport energy through snow. Snow densities were calculated as a function of depth, and other properties varied with density. For all snow, sea ice, and water surfaces, an additional layer was added to the bottom of the atmospheric radiative transfer calculation to solve for radiation fluxes through snow, ice, and water, respectively. The purpose of adding this layer was to predict, rather than prescribe, the albedo at the snow-air, ice-air, and water-air interface, particularly in the presence of pollutants such as black carbon, brown carbon, and soil dust.

Fig. S2 compares near-surface wind speed predictions at 4×5 degree resolution from the model with 1.5×1.5 degree resolution data over the oceans. Despite the nine times coarser resolution of the model relative to the data, the model picked up the main features of the data. Some other comparisons of model behavior over the ocean can be seen in figure 2 of ref. 11, which compares modeled monthly sea ice area over the Antarctic and Arctic with data, and figure 2 of ref. 12, which compares modeled zonally averaged (from the surface to 18 km) static stability with satellite data. Static stability accounts for the vertical temperature profile.

1. Jacobson MZ (2001) GATOR-GCMM: A global- through urban-scale air pollution and weather forecast model. 1. Model design and treatment of subgrid soil, vegetation, roads, rooftops, water, sea ice, and snow. *J Geophys Res* 106:5385–5402.
2. Jacobson MZ, Wilkerson JT, Naiman AD, Lele SK (2011) The effects of aircraft on climate and pollution. Part I: Numerical methods for treating the subgrid evolution of discrete size- and composition-resolved contrails from all commercial flights worldwide. *J Comp Phys*230:5115–5132.
3. Jacobson MZ, Ten Hoeve JE (2012) Effects of urban surfaces and white roofs on global and regional climate. *J Climate* 25:1028–1044.
4. Baidya Roy S, Pacala SW, Walko RI (2004) Can large wind farms affect local meteorology. *J Geophys Res*109:D19101.
5. Baidya Roy S (2011) Simulating impacts of wind farms on local hydrometeorology. *J Wind Eng Ind Aerod*. 99:491–498.
6. Masters GM (2004) *Renewable and Efficient Electric Power Systems*. John Wiley & Sons, Hoboken, NJ.
7. Mellor GL, Yamada T (1982) Development of a turbulence closure model for geophysical fluid problems. *Rev Geophys Space Phys* 20:851–875.
8. Global Forecast System (GFS) weather reanalysis fields (2010) National Oceanic and Atmospheric Administration, Available at http://nomads.ncdc.noaa.gov/data/gfs-avn-hi/. Accessed February 23, 2012.
9. Ketefian GS, Jacobson MZ (2009) A mass, energy, vorticity, and potential enstrophy conserving boundary treatment scheme for the shallow water equations. *J Comp Phys* 228:1–32.
10. Jacobson MZ (2005) Studying ocean acidification with conservative, stable numerical schemes for nonequilibrium air-ocean exchange and ocean equilibrium chemistry. *J Geophys Res* 110:D07302.
11. Jacobson MZ (2010) Short-term effects of controlling fossil-fuel soot, biofuel soot and gases, and methane on climate, Arctic ice, and air pollution health. *J Geophys Res* 115:D14209.
12. Whitt DB, Wilkerson JT, Jacobson MZ, Naiman AD, Lele SK (2011) Vertical mixing of commercial aviation emissions from cruise altitude to the surface. *J Geophys Res*, 116:D14109.

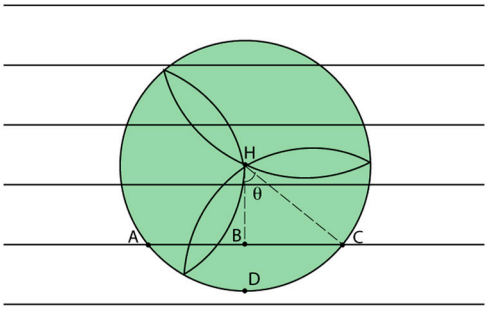

Fig. S1. Illustration of how the swept area of a single wind turbine intersects multiple model vertical layers in a single grid column. Points A, B, C, D, and H are discussed in the text.

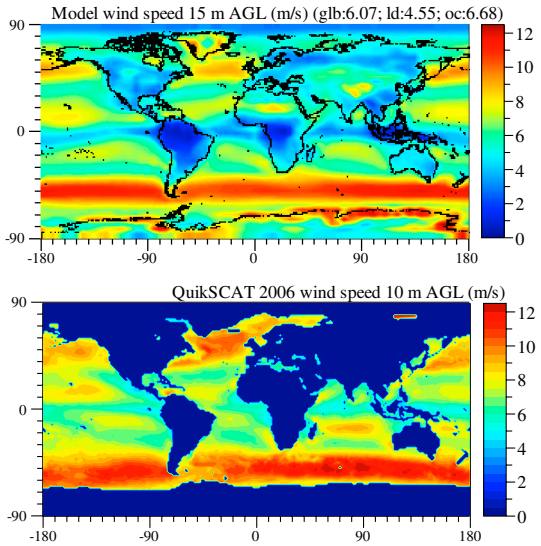

Fig. S2. Modeled 2006 15-m wind speed at 4×5 degree resolution vs. 10-m data at 1.5×1.5 degree resolution (1) for the same year.

1 *Quikscat* processed by Whitt D, Dvorak M (2010). Available at http://podaac.jpl.nasa.gov/DATA_CATALOG/quikscatinfo.html. Accessed February 23, 2012.

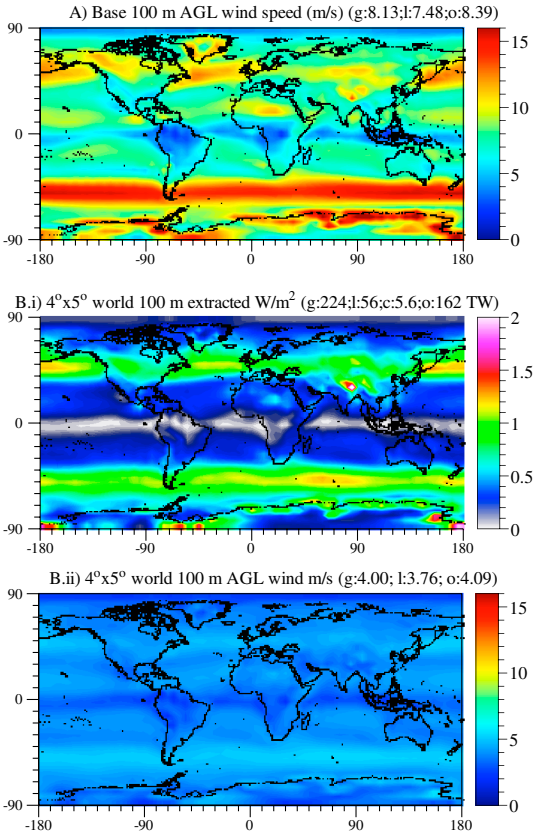
A) Base 100 m AGL wind speed (m/s) (g:8.13;l:7.48;o:8.39)
90
0
-90
-180
-90
0
90
180
15
10
5
0
B.i) 4°x5° world 100 m extracted W/m2 (g:224;l:56;c:5.6;o:162 TW)
2
1.5
1
0.5
0
B.ii) 4°x5° world 100 m AGL wind m/s (g:4.00; l:3.76; o:4.09)

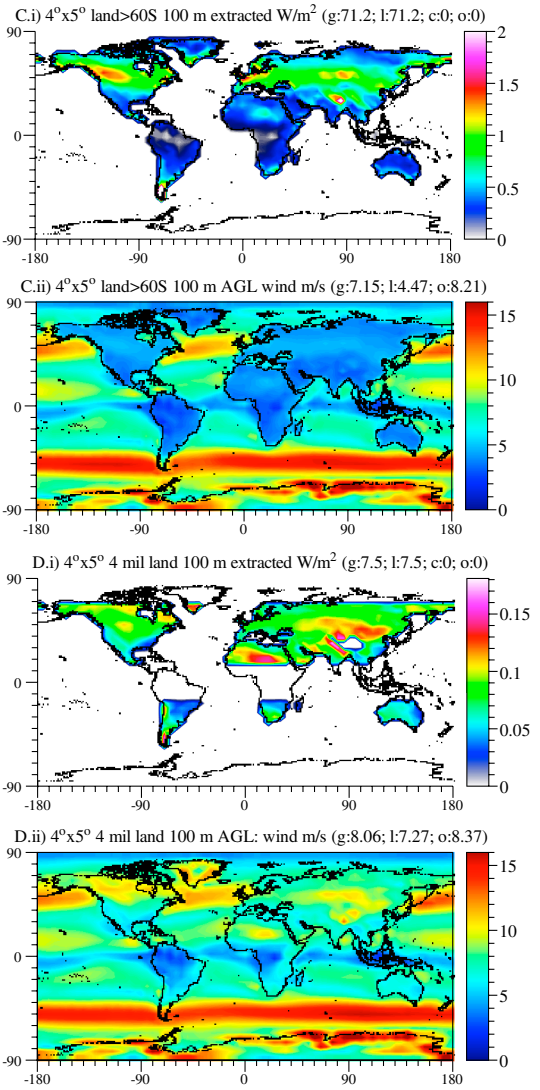
C.i) 4°x5° land>60S 100 m extracted W/m2 (g:71.2; l:71.2; c:0; o:0)
90
0
-90
-180
-90
0
90
180
2
1.5
1
0.5
0
C.ii) 4°x5° land>60S 100 m AGL wind m/s (g:7.15; l:4.47; o:8.21)
15
10
5
0
D.i) 4°x5° 4 mil land 100 m extracted W/m2 (g:7.5; l:7.5; c:0; o:0)
0.15
0.1
0.05
D.ii) 4°x5° 4 mil land 100 m AGL: wind m/s (g:8.06; l:7.27; o:8.37)

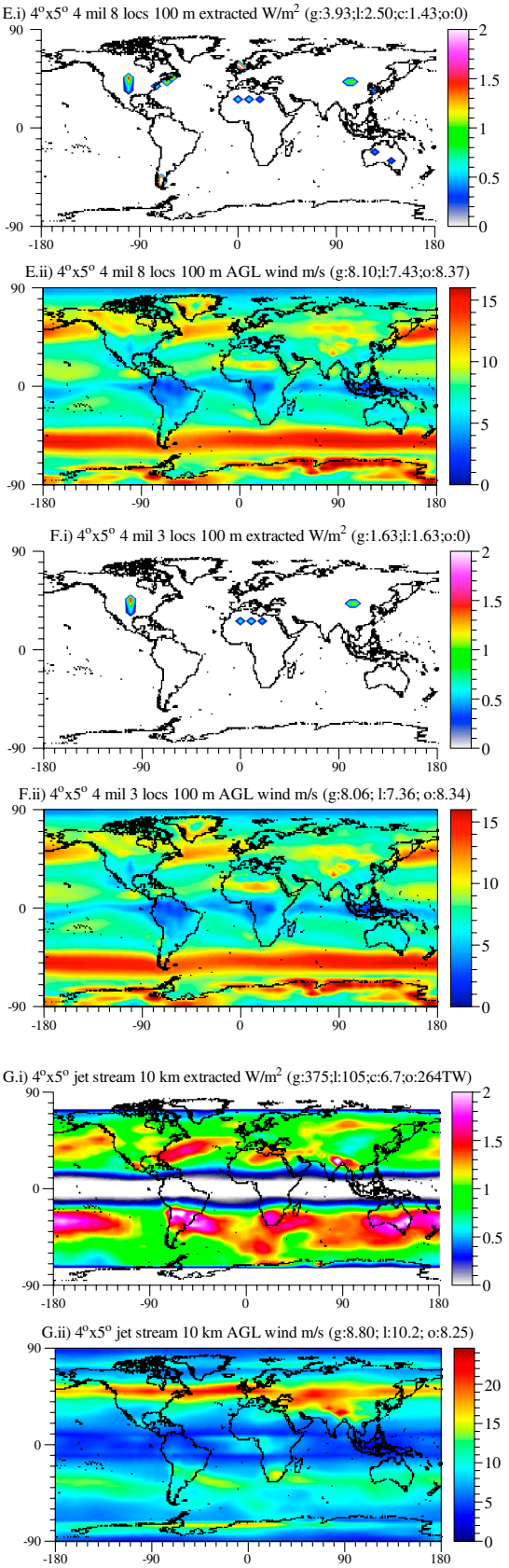

Fig. S3. (*A*) Modeled (4° × 5° horizontal resolution) annually-averaged (during the last year of simulation) 100-m wind speeds in the absence of wind turbine power extraction (Simulation A). (*B*) Same as (*A*) but for power (W/m^2) extracted from wind turbines (*i*) and the resulting wind speeds (m/s) (*ii*) accounting for worldwide turbine momentum extraction (Simulation B). (*C*) Same as (*B*) but for wind turbines over all land outside Antarctica (Simulation I). (*D*–*F*) Same as (*B*) but for the three cases of four million turbines (Simulation N–P), (*G*) Same as (*B*) but for turbine extraction in the jet stream at 10 km (Simulation Q). *g* = global average; *l* = land-average; *c* = average over coastal ocean (water with depth less than 200 m outside Antarctica), and *o* = average over all other ocean.

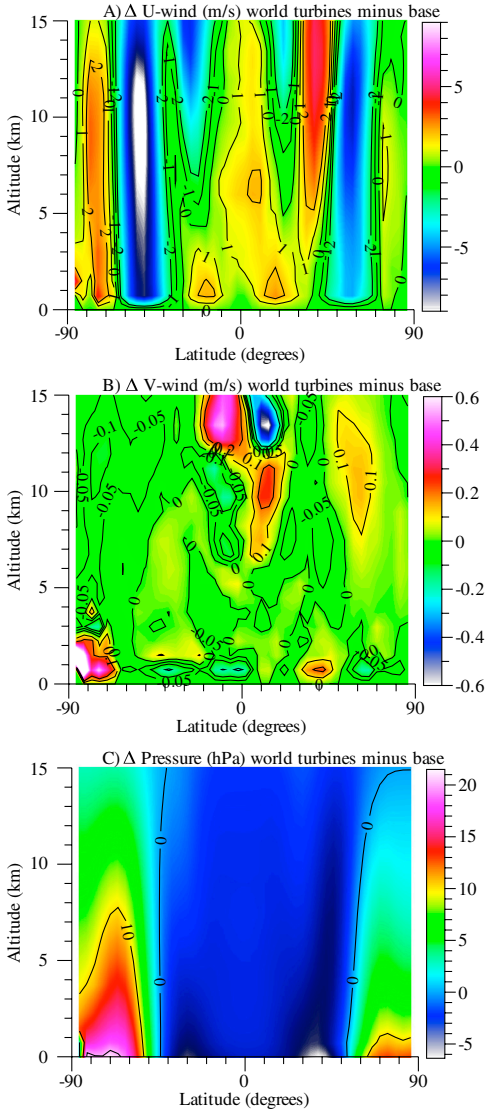

Fig. S4. Zonally averaged changes during the last simulation year in several meteorological variables between the global surface turbine case (Simulation B) and the base case (Simulation A).

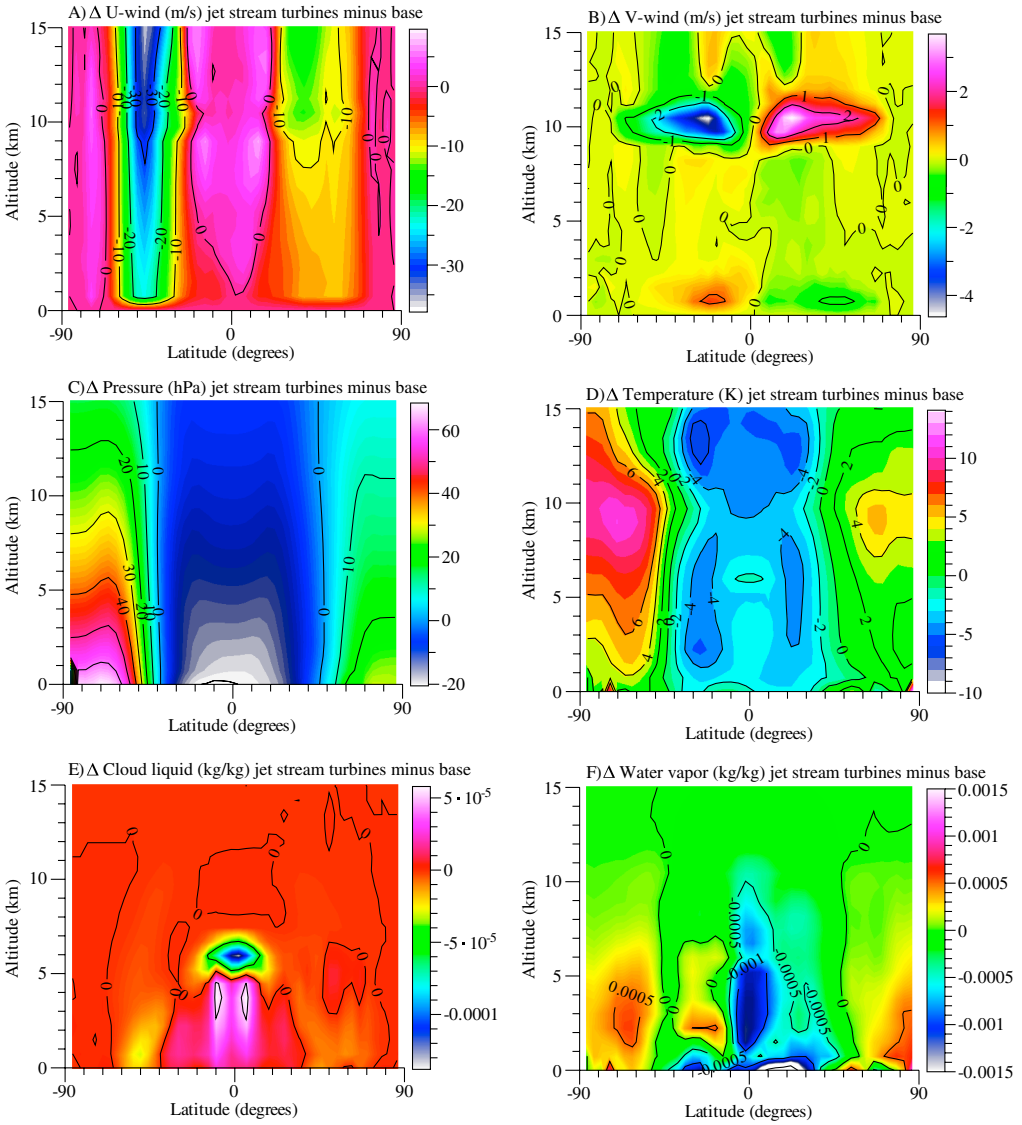

Fig. S5. Zonally averaged changes during the last simulation year in several meteorological variables between the case with turbines at 10 km (jet stream case, Simulation Q) and the base case (Simulation A).